Investigation of biochemical changes indicative of abnormal cervical remodeling during preterm birth using *in vivo* Raman spectroscopy

By

Jennifer N. Bateman

Thesis

Submitted to the Faculty of the

Graduate School of Vanderbilt University

in partial fulfillment of the requirements

for the degree of

MASTER OF SCIENCE

in

Biomedical Engineering

May 10, 2019

Nashville, Tennessee

Approved:

Anita Mahadevan-Jansen, Ph.D.

Jeff Reese, M.D.

ACKNOWLEDGEMENTS

I would like to thank the NIH whose funding made this work possible and my predecessors who tirelessly brought this work from an idea to reality.

I would also like to thank my advisor, Dr. Anita Mahadevan-Jansen, whose expertise I could not do without. I'd like to thank Dr. Jeff Reese for being an unofficial co-advisor treating me like his own student, Dr. Jen Herington for spending very late nights with me working on experiments and providing invaluable insight, and the Neonatology Department for being my lab away from lab.

I'd also like to thank the members of the Vanderbilt Biophotonics Center, who provided me with not only endless support, but also lifelong friendships. Specifically, I'd like to thank my fellow Ramanologists for providing me with a wealth of both knowledge and laughter.

Finally, I'd like to thank my family and Zachary Collins. Without their love and encouragement, none of this work would have been possible. Especially Zach, who made countless sacrifices and even more midnight food deliveries to lab to help me through even the toughest of times.

TABLE OF CONTENTS

LIST OF FIGURES

LIST OF TABLES

CHAPTER I

INTRODUCTION AND BACKGROUND

Cervix Biology

The cervix is the lowest portion of the uterus and is surrounded by the vaginal wall (Fig. 1) [5,7]. In nonpregnant adult women, the cervix is 3.5 cm in length and 2 cm in diameter. Columnar epithelium covers the portion of the cervix that protrudes into the vagina. The endocervical canal is lined by a single layer of glandular, mucus-secreting epithelial cells line that extend into the stroma as cervical crypts (Fig. 2) [5,7] while the rest of the cervix is covered by squamous cells [7]. Comprised of fibroblasts and smooth muscle cells, the cervical stroma is the primary source of structural proteins, collagen, and elastin [8]. The smooth muscle content of the stroma is organized in a gradient fashion from internal to external os [9]. The cervix is provided with a blood supply from the descending branch of the uterine artery and the vaginal artery [7]. This blood supply allows the cervix to heal from otherwise serious injuries.

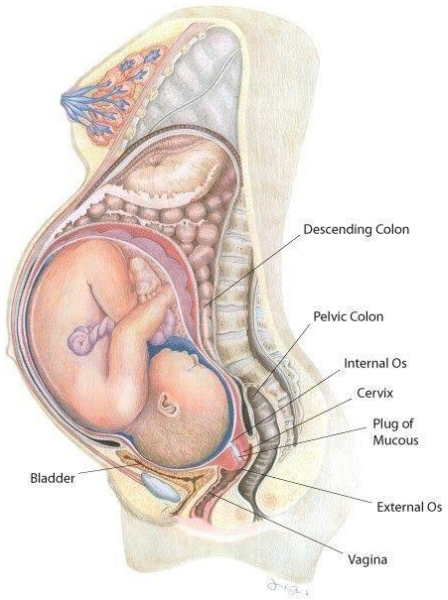

Figure 1. Diagram of the cervix during pregnancy [2]

Pregnant Cervix

The cervix acts as a barrier between the womb and the outside world [8,9]. In the cervix, tissue hydration, collagen structure, and tissue elasticity change throughout pregnancy as it undergoes a transformation to prepare the body for parturition. This transformation, termed cervical remodeling, includes four overlapping phases: softening, ripening, dilation, and

postpartum repair (Fig. 3) [4,6,9]. Each phase of cervical remodeling occurs in a dynamic and unique endocrine environment of epithelial, stromal, immune, and endothelial cells in addition to the structure of the extracellular matrix (ECM) [6] (Table 1). The cervix becomes softer and more compliant during cervical ripening but maintains structural integrity. During cervical ripening and dilation, tissue compliance reaches its maximum and the cervix loses structural integrity [8]. Cervical diameter increases while cervical length shortens and the wall of the cervix thins (Fig. 4) [7]. These alterations will allow the cervix to dilate to 10 cm, to

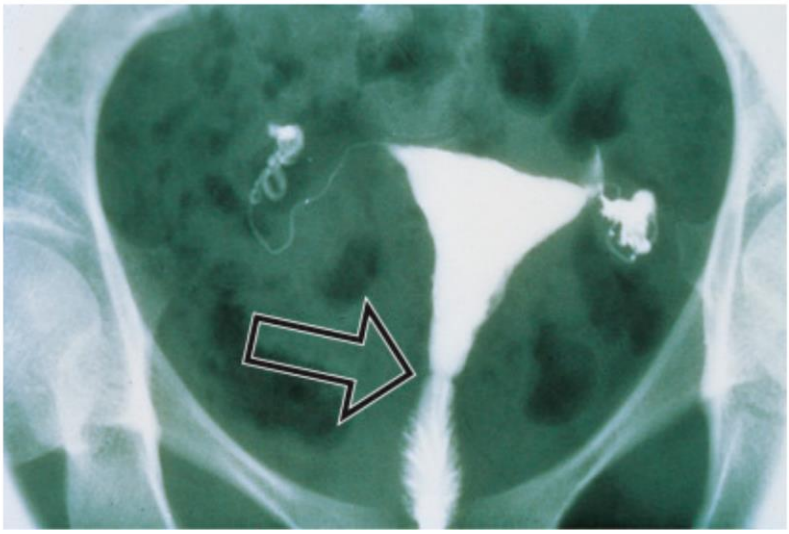

Figure 2. X-ray of the cervix pointing out the internal cervical os with an arrow and cervical crypts below extending into the stroma [7]

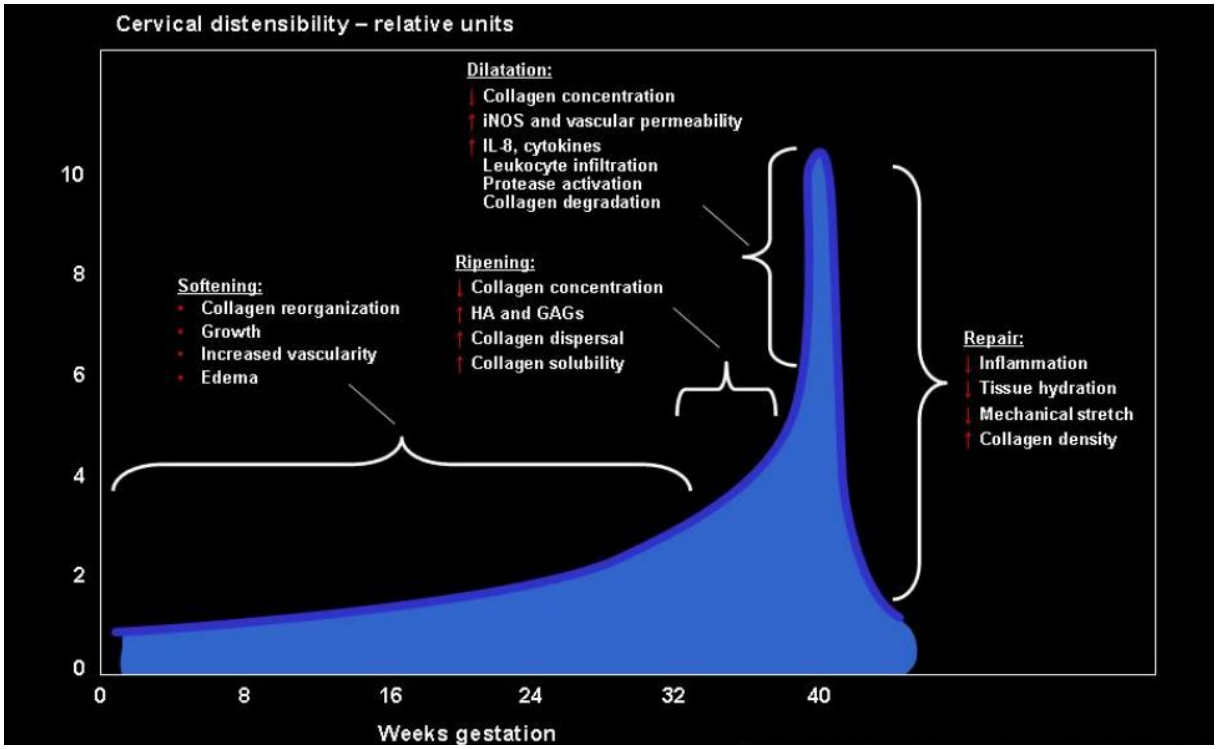

Figure 3. Phases of cervical remodeling [4]

accommodate passage of the fetal head and torso [7,8]. In parallel, blood supply to the cervix greatly increases providing a bluish appearance to the tissue.

Table 1. Phases of cervical remodeling [6]

Softening	Ripening/dilation	Postpartum repair
Slow, progressive phase	Rapid phases	↑ Synthesis of ECM molecules
↑ Progesterone function	↓ Progesterone function	↑ Metabolism of high MW HA to low MW HA
↓ Estrogen levels	↑ Estrogen levels	↑ Matricellular proteins
Changes in collagen structure (↓ crosslinking, ↑ solubility)	↑ Tissue hydration	↑ Proinflammatory gene expression
↑ Tissue growth	↑ High MW hyaluronan	↑ Neutrophils
↑ Epithelial repair and protective factors (Tff1, Spink 5)	Maximal ↓ of tensile strength	Activation of M1 and M2 macrophages
↓ Tensile strength	↑ Tissue monocytes ↑ Vascularization	

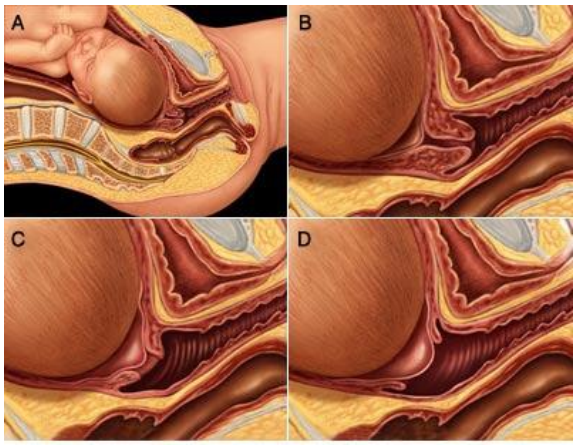

Figure 4. The cervix thins as parturition nears [3]

Cervical Softening

During cervical softening, mature cross-linked collagen is replaced by immature poorly cross-linked fibrils through downregulation of lysyl hydroxylase and lysyl oxidase. Matricellular proteins thrombospondin-1, thrombospondin-2, and tenascin C which are thought to play a role in maintaining rigidity of the cervix throughout pregnancy decrease in the cervix during pregnancy [4,8]. Relaxin, a hormone secreted by the placenta and uterine lining, also plays an important role in cervical softening by mediating vascular changes [10]. Softening occurs while the cervix is a progesterone-rich environment, which is thought to contribute to the relatively slow progression of cervical remodeling.

Cervical Ripening

Cervical ripening occurs during the last weeks of pregnancy in women and results in the cervix becoming thin and easily stretched. This is due to changes in the extracellular matrix (ECM) and cervical water content. During cervical ripening, cross-linked collagen fibrils tend to become unlinked and disorganized (Fig. 5). Unlike the softening phase, cervical ripening is an accelerated process that is achieved by a decline in progesterone function and increase in estrogen activity [9]. Substantial elevation of hydrophilic glycosaminoglycans (GAG) and non-collagenous proteins result in tissue hydration which consequently causes

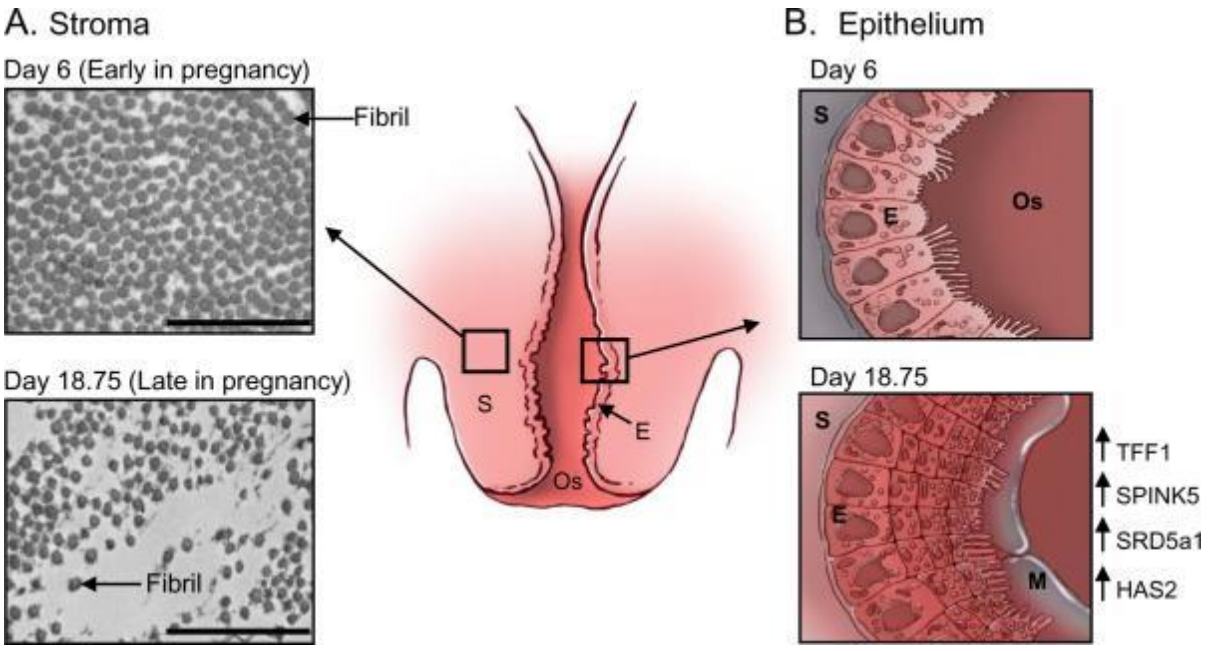

Figure 5. Changes in cervical stroma and epithelium during pregnancy [6]

increased collagen solubility increased susceptibility to endogenous proteases, and eventually higher disorder of the collagen fibers. While the mechanisms that induce collagen, solubility are not clearly understood, researchers currently postulate that hyaluronan may play a prominent role in collagen dispersal as hyaluronan levels were found to be notably increased during cervical ripening. Hyaluronan is a GAG found in the ECM of all mammalian tissues and is synthesized by cervical fibroblasts, epithelial cells, and immune cells. GAGs regulate macromolecular assembly in the ECM; hyaluronan in particular can promote increased viscosity, hydration, and matrix disorganization [8,11]. Furthermore, relaxin is thought to stimulate hyaluronan synthesis [12]. During the ripening phases, hyaluronan levels are increased and hyaluronan binds to the surface receptor CD44 stimulating macrophages to migrate to inflammation sites in the cervix. These macrophages in turn produce chemokines that initiate an inflammatory cascade that propagates collagen solubilization [4].

Cervical Dilation

Cervical dilation generally occurs days before delivery in women and hours before delivery in mice. [4,6]. As uterine contractions begin, it has been observed that the degree of cervical dilation correlates with an influx of matrix metalloproteases and leukocytes. Studies have since demonstrated that leukocyte collagenase is the major source of collagenase found

in the cervix during active labor. However, the mechanism that promotes or induces leucocyte recruitment during dilation is unknown at present, though it has been postulated that S100A9 may have a contributory role [4].

Postpartum Repair

Postpartum repair occurs after delivery which allows the cervix to return to its original role as a functioning barrier and the process has been likened to the structural changes observed in wound healing. As a result, collagen cross-links reform as matrix cross-linking and collagen synthesis genes are upregulated [13].

Preterm Birth

PTB is defined as birth between 20 and 37 weeks of gestation [5,14]. On that basis, PTB is highly prevalent in the US with one in ten infants being born premature [15]. PTB is also associated lower survival rates and higher complications because premature infants are at a higher risk of infections and development issues including cerebral palsy, respiratory morbidity, mental retardation, blindness, deafness, cardiovascular disease and cancer [16,17]. Due to these factors, the high prevalence of PTB has resulted in costs as high as $26 billion, causing a burden on the American healthcare system. Despite medical advancements in the recent decades, incidence of PTB continues to rise and is estimated to have increased 35% in the last 25 years. In addition, half of all PTB cases occur in women with no known clinical risk factors where the PTBs are unexplained, or spontaneous [16].

Among the known causes of PTB, several etiological factors have been considered: cervical infection, placental vascular complications, maternal fatigue due to stress and work strain, and uterine stretch due to multiple gestations (Fig. 6)[5]. The etiology of PTB is complex as it could be associated with various risk factors, such as a history or previous PTB, the current most accurate indicator of future incidences. PTB risks also include racial disparity that is only partially explained by socioeconomic factors [16,17]. Other important risk factors include a family history of PTB, child abuse, smoking or exposure to second hand smoke,

substance abuse, a history of early pregnancy losses, previous cervical surgery, obesity, hypertension, and diabetes [5]. In addition to the aforementioned risk factors, several biomarkers have been identified that could help predict PTB including fetal fibronectin [18], salivary estriol, corticotrophin releasing hormones, interleukin-6, C-reactive protein, CD163 8, ferritin, placental alkaline phosphates, relaxin, and cervical length [16]. However, intervention based on screening for these biomarker profiles have not demonstrated the ability to reduce the risk of PTB because successful predictions using these biomarkers tend to predominantly occur in patients with a prior history of PTB.

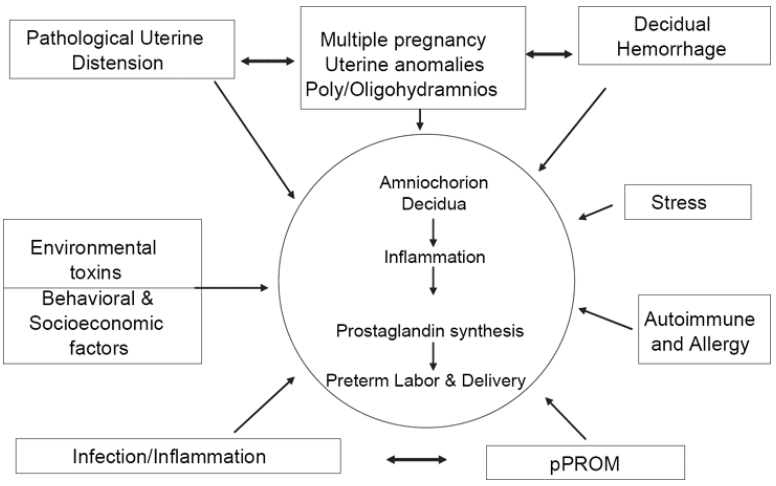

Figure 6. Etiological factors of PTB [5]

Current Diagnostic Methods of PTB

In order to detect onset of PTB, frequency of uterine contractions (if any) and cervical length and dilation are monitored periodically during prenatal visit. Cervical dilation is assessed using the Bishop score, a manual evaluation of the cervix and fetal head position using a physical examination (Table 2) [5]. While cervical length is currently the most often used indicator for PTB risk, several studies have now provided contradictory findings regarding the role of cervical length in PTB [18]. In fact, most nulliparous women with a short

Table 2. Bishop score guidelines

Physical Findings	Rating			
	0	1	2	3
Cervix				
Position	Posterior	Mid	Anterior	—
Consistency	Firm	Medium	Soft	—
Effacement (%)	0-30	40-50	60-70	≥80
Dilation (cm)	0	1-2	3-4	≥5
Fetal Head				
Station	−3	−2	−1	+1

cervix still deliver at term [17]. In addition to cervical parameters, clinicians also send out routine laboratory investigation to rule out urinary tract or vaginal infections, which could cause inflammation that could trigger PTB.

Diagnostic Modalities Used to Study PTB

Ultrasound Imaging

Cervical ultrasonic attenuation (the loss of ultrasound signal with depth) has been suggested as a better predictor of PTB. [17,19]. However, researchers who adopted this prediction model based it on the assumption that the cervix is a homogeneous tissue in their predictions, which is not the case as discussed previously. In addition to cervical attenuation, ultrasound backscatter due to scatterers such as collagen has been shown to change with respect to the incident angle of the acoustic beam and tends correlate with collagen fiber organization and orientation. However, this technique requires the user to map out the entire cervix to determine location, making it impractical in the clinic in its current state. Ultrasound has also been used to obtain a measurement of cervical compression potential (cervical consistency index), which is based on the differences in echogenicity of the posterior and anterior cervix can be indicative of the "hardness" of a cervix. In a previous study, preterm birth was predicted at <32 weeks, <34 weeks, and <37 weeks, but the respective sensitivities were low (67%, 64%, 45%) [20]. Tissue deformability is another tissue property that could serve as an indicator for cervical ripening. Elastography, a method that also uses a transducer to deform the tissue, produces a color map that describes the motion of tissue relative to neighboring areas. Researchers saw potential in this technique, but decide that the reproducibility of this approach is uncertain as there is no means for standardization and minimization of variability [21]. Despite a lack of standardization, one study of 700 pregnant women showed that soft and medium soft cervices as determined by elastography were associated with significantly higher rates of PTB [20]. Because acoustic waves travel more slowly in softer tissue, shear wave speed can be measured to determine level of cervical ripening. However, a specialized software and transducer are required to obtain images [17]. Researches have also attempted to use sonography to measure cervical

gland area as a predictor of cervical remodeling. However, studies have revealed that no trend was observed in cervical gland area whether women delivered PTB or at term, which a major disadvantage of this technique being that it suffered from subjectivity in image interpretation [4,17].

Other Techniques

In the past, researchers have identified several methods to evaluate microstructural changes during cervical remodeling. *Based on en face* images of the cervix, researchers observed that while the cervix area increased throughout pregnancy, the folds of the cervix made it difficult to calculate an accurate surface area [22]. Other parameters such as tissue hydration that could be indicative of cervical remodeling have been demonstrated to correlate with electrical impedance of the tissue, though researchers were unable to gather significant predictive results using this method [23,24]. In comparison, MRI has been used to study stromal differentiation and correlated with cervical length, but predictive results were on par with that obtained by ultrasound [17,18,25]. Researchers have attempted to quantify tissue deformity by using the aspiration technique, which uses a vacuum to stretch the cervix to 4mm of deformation while recording tension. While statistically significant differences were seen between the 1st and 2nd trimester, researchers were unable to determine significant differences of the tissue between the 2nd and 3rd trimester [20].

Optical Techniques

Since studies have demonstrated that collagen cross-linking decreases during cervical remodeling, researchers have attempted to use light-induced fluorescence to detect the autofluorescence of cross-linked collagen in the cervix. Fluorescence was inversely correlated with gestational age, and correlated with time to delivery, but the correlations were relatively weak [26]. On the other hand, second harmonic generation endomicroscopy has been found to be capable of quantifying changes in cervical morphology throughout gestation *ex vivo*, but remains to be validated *in vivo* [17,27,28]. While the described imaging techniques could offer an insight intro structural changes that occur during cervical remodeling, these modalities only provide a limited insight regarding biochemical changes. Raman spectroscopy has been demonstrated as a viable method to assess cervical

remodeling, where changes in ECM proteins, blood, actin, and cholesterol could be detected using this technique [29,30].

Raman Spectroscopy

Though the Raman effect was discovered in 1928, the first laser-equipped Raman spectroscopy instrument was not created until 1962 [31]. The Raman effect refers to inelastic scattering of a photon by the molecular bonds as the result of monochromatic excitation. This excites the molecule into a virtual energy state. The molecule then relaxes back to its ground electronic state consequently releasing energy in the form of light that is collected by a detector. The exchange of energy between photons and molecular bond vibrations gives rise to an anti-Stokes and Stokes signals. If the resultant energy released is more than the energy used to shift to a virtual state, the phenomena is called anti-Stokes Raman scattering. However, this phenomenon is very weak at room temperature compared to Stokes Raman scattering where the resultant energy released is less than the incident energy (Fig. 7). Stokes Raman scattering will be interrogated in this study to understand changes in molecular bond vibrations upon cervical remodeling. Accounting for only 1 in every 10 million photons, Raman scattering is a highly weak signal and must be separated from the other light phenomenon occurring simultaneously such as fluorescence.

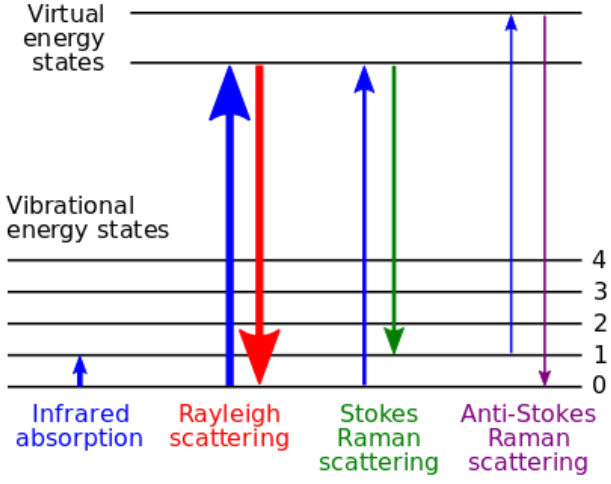

Figure 7. Jablonski diagram showing energy state changes due to scattering [1]

To build a Raman spectroscopy system, a source, sampling apparatus, and a detector are needed. The source must consist of monochromatic light, usually a laser. The light is projected onto a sample and the resultant scattered light is collected via a fiber optic probe or optical objective lens. The light is sent through a small slit and then directed

onto a prism or grating to separate the light according to wavelength. The dispersed light is projected onto a detector where pixels correspond to wavelengths. Because Raman scattering is a relatively weak signal, Raman spectrometers are designed to be efficient requiring narrow bandpass filters to reduce unwanted light input, highly sensitive, cooled detectors to reduce thermal noise and few elements in between to reduce loss of light [1].

Application of Raman Spectroscopy in Medicine

For biochemical applications, near infrared light has been used as an excitation source because it minimizes the effect of fluorescence and reduces photodamage. To achieve the optimum balance between fluorescence reduction and increased spectral resolution, 785nm diode lasers have become a standard excitation source for biological applications (Fig. 8)[1].

Several studies have already demonstrated the potential of *in vivo* Raman spectroscopy as a viable optical tool to detect disease and study biological responses. Raman spectroscopy has also been widely applied to study cancer of multiple organs such as the gastrointestinal tract, where cancer of the oral cavity was detected with over 70% accuracy [32,33]. While the oral cavity is an easily accessible organ for Raman spectroscopic measurements, it becomes more challenging to apply this technique to cancers of other organs of the gastrointestinal tract. To solve this challenge, recent trends have led to Raman spectroscopy relying on fiber optics to ensure compatibility with an endoscopic probe to gain access to visceral organs such as the stomach, esophagus, and colon. The diagnostic potential of probe-based Raman spectroscopy has since been

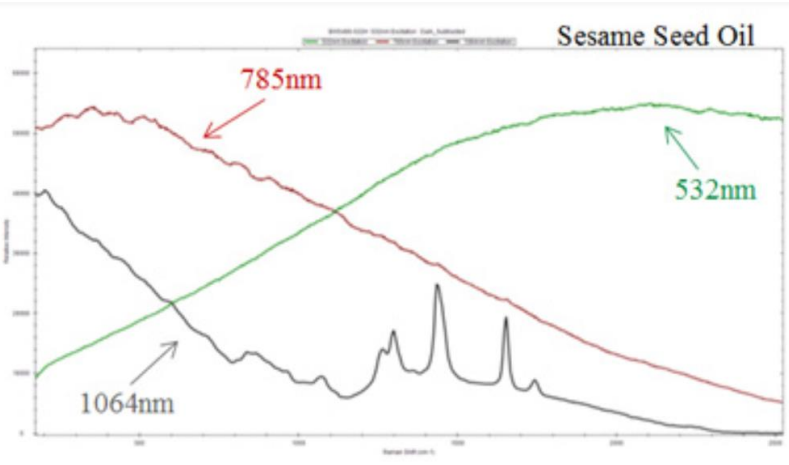

Figure 8. Effect of excitation source in Raman

demonstrated for detection of cancers in skin [34], esophagus in asymptomatic patients [33,35-37], stomach (precancer) [33,38], bladder, prostate [39,40], and breast [41]. In addition to malignancies, Raman has also been used to study inflammatory bowel disease by interrogating the colon with a colonoscopy coupled Raman probe [42]. Probe-based Raman spectroscopy has also been applied to assessing skin hydration by measuring the spectra in the high wavenumber region [43,44].

In vivo Raman spectroscopy has already been extensively applied to studying the cervix, with original studies beginning as early as 1998 [45]. Raman spectroscopy was used to distinguish low and high grade squamous intraepithelial lesions, metaplasia and normal cervical tissue in vivo [46]. Raman has also been used to detect precancerous conditions such as human papillomavirus, which can lead to cervical cancer [47,48]. In addition to traditional near infrared Raman spectroscopy in the fingerprint region (500-1800 cm^{-1}), high wavenumber (2600-3800 cm^{-1}) Raman has been shown to improve cervical precancer detection [49]. Recently, Raman spectroscopy has proved a valuable tool to study pregnancy[29,30,50-55].

Objectives

The goal of this study is to determine biochemical differences between normal and abnormal cervical remodeling. Normal delivery mouse models will be assessed to gather a baseline of expected biochemical changes. PTB models will then be studied to determine discrepancies between expected results. Finally, inflammation-mediated and induced PTB models will be compared to determine if it is possible to differentiate between different etiologies associated with PTB because intervention methods rely on knowing the cause. Understanding the nuances of cervical remodeling would provide more information to base PTB predictions on and would aid researchers in determining pathways that are likely to respond well to intervention.

In keeping in line with the described objectives, mice will be used as an animal model to study cervical remodeling as described in the next chapter because the mouse cervix follows a similar pattern to women [29,56]. Cervical softening occurs in the first trimester for

humans and day 11 of a 19-day gestation for mice. Unlike ripening and dilation, cervical softening is a slow process. During softening, the cervix develops increased vascularity and swelling and undergoes hypertrophy of the stroma and cervical crypts, and hyperplasia of the crypts. By the end of pregnancy, 50% of the cervical mass is comprised of endocervical crypts. The epithelial cells that invaginate into the crypts serve the purpose of secreting a thick mucus to protect the uterus from invading microorganisms. Furthermore, they mediate inflammatory responses to limit bacterial proliferation. Studies indicate that these epithelial cells promote progesterone upregulation in tissue and play an important role in cervical remodeling. Cervical ripening is required for delivery, even in PTB models. Across multiple animal models, cervical integrity is maintained until late pregnancy [4].

References

1. Bwtek. Components of a Raman Spectrometer. 2019.
2. Zone TP. 40 Weeks Pregnant. 2019; https://www.thepregnancyzone.com/pregnancy-weeks/40-weeks-pregnant/.
3. Clinic M. Cervical effacement and dilation. 2019; https://www.mayoclinic.org/healthy-lifestyle/labor-and-delivery/multimedia/cervical-effacement-and-dilation/img-20006991.
4. Word RA, Li X-H, Hnat M, Carrick K. Dynamics of cervical remodeling during pregnancy and parturition: mechanisms and current concepts. Paper presented at: Seminars in reproductive medicine2007.
5. *Hacker & Moore's essentials of obstetrics and gynecology.* Sixth edition. ed. Philadelphia, PA: Elsevier; 2016.
6. Timmons B, Akins M, Mahendroo M. Cervical remodeling during pregnancy and parturition. *Trends in Endocrinology and Metabolism.* 2010;21(6):353-361.
7. Baggish MS. *Atlas of pelvic anatomy and gynecologic surgery.* Fourth edition. ed. Philadelphia, PA: Elsevier; 2016.
8. Mahendroo M. Cervical hyaluronan biology in pregnancy, parturition and preterm birth. *Matrix Biology.* 2017.
9. Nallasamy S, Mahendroo M. Distinct Roles of Cervical Epithelia and Stroma in Pregnancy and Parturition. *Seminars in Reproductive Medicine.* 2017;35(2):190-199.
10. Irani RA, Foster S. Overview of the mechanisms of induction of labor. *Seminars in Perinatology.* 2015;39(6):426-429.
11. Akgul Y, Holt R, Mummert M, Word A, Mahendroo M. Dynamic changes in cervical glycosaminoglycan composition during normal pregnancy and preterm birth. *Endocrinology.* 2012;153(7):3493-3503.

12. Jelinic M, Marshall SA, Leo CH, Parry LJ, Tare M. From pregnancy to cardiovascular disease: Lessons from relaxin-deficient animals to understand relaxin actions in the vascular system. *Microcirculation.* 2019;26(2).
13. Timmons BC, Mahendroo MS. Timing of neutrophil activation and expression of proinflammatory markers do not support a role for neutrophils in cervical ripening in the mouse. *Biol Reprod.* 2006;74(2):236-245.
14. Narice BF, Green NH, MacNeil S, Anumba D. Second Harmonic Generation microscopy reveals collagen fibres are more organised in the cervix of postmenopausal women. *Reproductive Biology and Endocrinology.* 2016;14(1):70.
15. Centers for Disease Control and Prevention. Preterm Birth. 2018; https://www.cdc.gov/reproductivehealth/maternalinfanthealth/pretermbirth.htm.
16. Menon R. Spontaneous preterm birth, a clinical dilemma: etiologic, pathophysiologic and genetic heterogeneities and racial disparity. *Acta Obstet Gynecol Scand.* 2008;87(6):590-600.
17. Feltovich H, Hall TJ, Berghella V. Beyond cervical length: emerging technologies for assessing the pregnant cervix. *Am J Obstet Gynecol.* 2012;207(5):345-354.
18. Son M, Miller ES. Predicting preterm birth: Cervical length and fetal fibronectin. *Seminars in Perinatology.* 2017;41(8):445-451.
19. McFarlin B, Bigelow T, Laybed Y, O'Brien W, Oelze M, Abramowicz J. Ultrasonic attenuation estimation of the pregnant cervix: a preliminary report. *Ultrasound in Obstetrics & Gynecology.* 2010;36(2):218-225.
20. Feltovich H, Carlson L. New techniques in evaluation of the cervix. *Semin Perinatol.* 2017;41(8):477-484.
21. Molina FS, Gomez LF, Florido J, Padilla MC, Nicolaides KH. Quantification of cervical elastography: a reproducibility study. *Ultrasound in obstetrics & gynecology : the official journal of the International Society of Ultrasound in Obstetrics and Gynecology.* 2012;39(6):685-689.
22. Kuon RJ, Shi SQ, Maul H, et al. A novel optical method to assess cervical changes during pregnancy and use to evaluate the effects of progestins on term and preterm labor. *Am J Obstet Gynecol.* 2011;205(1):82.e15-20.
23. O'Connell MP, Tidy J, Wisher SJ, Avis NJ, Brown BH, Lindow SW. An in vivo comparative study of the pregnant and nonpregnant cervix using electrical impedance measurements. *BJOG : an international journal of obstetrics and gynaecology.* 2000;107(8):1040-1041.
24. Predanic M. Evaluation of a device for objective determination of cervical consistency: a pilot study of device's validity on uterine specimens obtained by total abdominal hysterectomy for benign uterine disease. *Journal of perinatal medicine.* 2002;30(5):364-366.
25. de Tejada BM, Faltin DL, Kinkel K, Guittier MJ, Boulvain M, Irion O. Magnetic resonance imaging of the cervix in women at high risk for preterm delivery. *The journal of maternal-fetal & neonatal medicine : the official journal of the European Association of Perinatal Medicine, the Federation of Asia and Oceania Perinatal Societies, the International Society of Perinatal Obstet.* 2011;24(11):1392-1397.
26. Maul H, Olson G, Fittkow CT, Saade GR, Garfield RE. Cervical light-induced fluorescence in humans decreases throughout gestation and before delivery:

preliminary observations. *American Journal of Obstetrics and Gynecology.* 2003;188(2):537-541.
27. Akins ML, Luby-Phelps K, Mahendroo M. Second harmonic generation imaging as a potential tool for staging pregnancy and predicting preterm birth. *Journal of Biomedical Optics.* 2010;15(2):026020-026020.
28. Zhang Y, Akins ML, Murari K, et al. A compact fiber-optic SHG scanning endomicroscope and its application to visualize cervical remodeling during pregnancy. *Proceedings of the National Academy of Sciences.* 2012;109(32):12878-12883.
29. O'Brien CM, Herington JL, Brown N, et al. In vivo Raman spectral analysis of impaired cervical remodeling in a mouse model of delayed parturition. *Sci Rep.* 2017;7(1):6835.
30. O'Brien CM, Vargis E, Rudin A, et al. In vivo Raman spectroscopy for biochemical monitoring of the human cervix throughout pregnancy. *Am J Obstet Gynecol.* 2018;218(5):528 e521-528 e518.
31. Ferraro JR, Nakamoto K, Brown CW. *Introductory Raman Spectroscopy.* San Diego, UNITED STATES: Elsevier Science & Technology; 2003.
32. Singh SP, Deshmukh A, Chaturvedi P, Murali Krishna C. In vivo Raman spectroscopic identification of premalignant lesions in oral buccal mucosa. *J Biomed Opt.* 2012;17(10):105002.
33. Pence I, Mahadevan-Jansen A. Clinical instrumentation and applications of Raman spectroscopy. *Chem Soc Rev.* 2016;45(7):1958-1979.
34. Lui H, Zhao J, McLean D, Zeng H. Real-time Raman Spectroscopy for In Vivo Skin Cancer Diagnosis. *Cancer Research.* 2012;72(10):2491-2500.
35. Barr H, Kendall C, Bazant-Hegemark F, Moayyedi P, Shetty G, Stone N. Endoscopic screening and surveillance for Barrett's esophagus--clinical implications. *MedGenMed.* 2006;8(2):88.
36. Shetty G, Kendall C, Shepherd N, Stone N, Barr H. Raman spectroscopy: elucidation of biochemical changes in carcinogenesis of oesophagus. *Br J Cancer.* 2006;94(10):1460-1464.
37. Bergholt MS, Zheng W, Lin K, et al. Characterizing variability in in vivo Raman spectra of different anatomical locations in the upper gastrointestinal tract toward cancer detection. *J Biomed Opt.* 2011;16(3):037003.
38. Huang Z, Teh SK, Zheng W, et al. In vivo detection of epithelial neoplasia in the stomach using image-guided Raman endoscopy. *Biosens Bioelectron.* 2010;26(2):383-389.
39. Grimbergen MC, van Swol CF, van Moorselaar RJ, Uff J, Mahadevan-Jansen A, Stone N. Raman spectroscopy of bladder tissue in the presence of 5-aminolevulinic acid. *J Photochem Photobiol B.* 2009;95(3):170-176.
40. Crow P, Molckovsky A, Stone N, Uff J, Wilson B, WongKeeSong LM. Assessment of fiberoptic near-infrared raman spectroscopy for diagnosis of bladder and prostate cancer. *Urology.* 2005;65(6):1126-1130.
41. Bhattacharjee T, Fontana LC, Raniero L, Ferreira-Strixino J. In vivo Raman spectroscopy of breast tumors prephotodynamic and postphotodynamic therapy. *Journal of Raman Spectroscopy.* 2018;49(5):786-791.

42. Pence IJ, Beaulieu DB, Horst SN, et al. Clinical characterization of in vivo inflammatory bowel disease with Raman spectroscopy. *Biomed Opt Express.* 2017;8(2):524-535.
43. Chrit L, Bastien P, Sockalingum GD, et al. An in vivo randomized study of human skin moisturization by a new confocal Raman fiber-optic microprobe: assessment of a glycerol-based hydration cream. *Skin pharmacology and physiology.* 2006;19(4):207-215.
44. Masson LE, O'Brien CM, Pence IJ, et al. Dual excitation wavelength system for combined fingerprint and high wavenumber Raman spectroscopy. *Analyst.* 2018;143(24):6049-6060.
45. Mahadevan-Jansen A, Mitchell MF, Ramanujam N, Utzinger U, Richards-Kortum R. Development of a Fiber Optic Probe to Measure NIR Raman Spectra of Cervical Tissue In Vivo. *Photochemistry and Photobiology.* 1998;68(3):427-431.
46. Kanter E, Vargis E, Majumder S, et al. Application of Raman spectroscopy for cervical dysplasia diagnosis. *Journal of Biophotonics.* 2009;2.
47. Vargis E, Tang Y-W, Khabele D, Mahadevan-Jansen A. Near-infrared Raman Microspectroscopy Detects High-risk Human Papillomaviruses. *Translational Oncology.* 2012;5(3):172-179.
48. Jess PRT, Smith DDW, Mazilu M, Dholakia K, Riches AC, Herrington CS. Early detection of cervical neoplasia by Raman spectroscopy. *International Journal of Cancer.* 2007;121(12):2723-2728.
49. Duraipandian S, Zheng W, Ng J, Low JJH, Ilancheran A, Huang Z. Effect of hormonal variation on in vivo high wavenumber Raman spectra improves cervical precancer detection. In*.* Vol 82142012:82140A-82140A-82146.
50. Vargis E, Brown N, Williams K, et al. Detecting Biochemical Changes in the Rodent Cervix During Pregnancy Using Raman Spectroscopy. *Annals of Biomedical Engineering.* 2012;40(8):1814-1824.
51. O'Brien CM, Vargis E, Slaughter C, et al. Characterization of human cervical remodeling throughout pregnancy using in vivo Raman spectroscopy. *Proc Spie.* 2015;9303.
52. O'Brien CM, Herrington J, Vargis E, et al. In Vivo Raman Spectroscopy Determines Biochemical Differences in the Pregnant Cervix of COX-1 KO Mice Are Responsible for Parturition Failure. *Reprod Sci.* 2014;21(3):335a-335a.
53. O'Brien C, Vargis E, Borwn N, Reese J, Paria BC, Mahadevan-Jansen A. In Vivo Detection of Biochemical Change in the Pregnant Cervix in Humans and Mouse Models. *Reprod Sci.* 2013;20(S3):240a-240a.
54. O'Brien CM, Vargis E, Paria BC, Bennett KA, Mahadevan-Jansen A, Reese J. Raman spectroscopy provides a noninvasive approach for determining biochemical composition of the pregnant cervix in vivo. *Acta Paediatrica.* 2014;103(7):715-721.
55. O'Brien CM, Brown N, Rudin A, et al. Detection of Biochemical Changes in the Cervix During Induction of Labor in Human Subjects and Mouse Models Using In Vivo Raman Spectroscopy. *Reprod Sci.* 2016;23:215a-215a.
56. Read CP, Word RA, Ruscheinsky MA, Timmons BC, Mahendroo MS. Cervical remodeling during pregnancy and parturition: Molecular characterization of the softening phase in mice. *Reproduction.* 2007;134(2):327-340.

Chapter II

RAMAN SPECTROSCOPY TO STUDY THE CERVIX IN TERM AND PRETERM MODELS

Introduction

Affecting 15 million infants per year, PTB is the leading cause of death for children under 5 years of age. Many etiological factors can cause PTB including infection/inflammation and progesterone inhibition [8]. While cervical remodeling and uterine contraction are essential for normal parturition, premature occurrence of cervical remodeling could lead to PTBs. Therefore, a pivotal insight regarding the etiology of PTB can be gained by studying the fundamental changes that occur during cervical remodeling, of which the mechanism is still not fully understood. Cervical remodeling is the process that the cervix undergoes to become thinner and shorter to allow passage of the fetus during birth and consists of four phases: softening, ripening, dilation, and postpartum repair. During cervical softening, the cervix becomes more vascularized and compliant while maintaining structural integrity during the majority of pregnancy. Conversely, cervical ripening is an accelerated process that occurs in the weeks leading up to pregnancy. During cervical ripening, water content of the cervix increases causing cross-linked collagen fibrils to unlink and become disorganized, weakening the structure of the ECM and allowing the cervix to dilate. Having a better understanding of the biochemical changes occurring during the phases of cervical remodeling would lead to better methods for predicting preterm birth.

Current diagnostic methods of PTB include assessing cervical length, monitoring for urinary tract or vaginal infections, tracking frequency of uterine contractions, and examining cervical dilation. Cervical dilation is assessed through physical examination of the cervix and fetal head position and then assigning a rating called the Bishop score which determines the probability that induction of labor will result in vaginal delivery [5]. Though the Bishop score is the standard practice in clinic, it is a subjective method that is limited by the level of experience of the practitioner and only assesses structural changes of the cervix on a macro scale. Ultrasound has been studied extensively as a method to predict preterm birth, but inherent limitations in standardization and low sensitivity have delayed its use in the clinic

for that purpose. Furthermore, ultrasound focuses on detecting structural changes of the cervix such as cervical length, but many patients with clinically short cervix still deliver at term [9].

Optical techniques such as fluorescence imaging and second harmonic generation have the ability to detect structural changes of the cervix but offer no insight to the biochemical changes that occur during cervical remodeling. Raman spectroscopy is a highly specific optical method that utilizes the vibrational modes of molecules and has been previously shown to be a viable method to study the biochemical properties of the cervix. Near infrared Raman spectroscopy has been used *in vivo* to detect precancerous conditions leading to cervical cancer[10] in addition to pregnancy in women and delayed parturition[11] mice. Current Raman studies of mouse cervices have been limited by interference from surrounding tissue which contains rich lipid signals and inherent weakness of Raman scattering in comparison to other simultaneous optical phenomena. An improved method that limits interfering extraneous signals while maintaining sensitivity would allow for a more in-depth study of the biochemical changes and upstream factors that could prelude PTB. This study aims to use a modified Raman spectroscopy probe to study differences in cervical remodeling between at term and preterm birth. Abnormal cervical remodeling of infection-mediated and induced preterm birth mouse models was studied and compared to normal wildtype mice.

Methods

Raman Spectroscopy System

Raman spectra were obtained using a probe-based portable Raman system. A 785nm diode laser delivered light to the sample through a coupled fiber optic probe. Raman signal was collected through the probe and traveled through a Kaiser imaging spectrograph to a CCD detector. The thermoelectrically cooled, back illuminated Pixies 256 CCD was connected to a computer with a LabVIEW GUI to adjust image acquisition parameters.

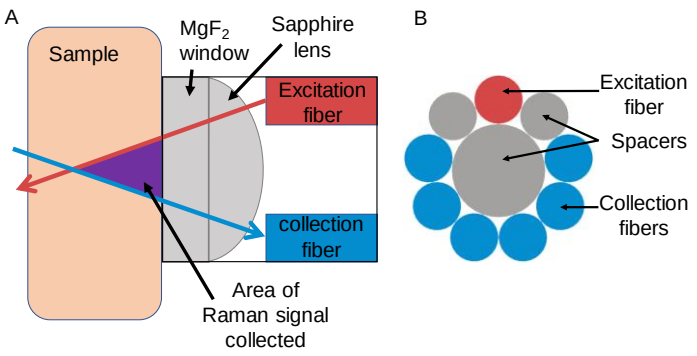

Figure 9. Shallow focus probe at (A) cross sectional and (B) en face view

In previous studies, the Raman spectra of the cervix showed a primarily lipid rich signal which overwhelmed valuable information about the biochemical composition of the changing pregnant mouse cervix [11]. A new shallow-focused probe was developed that minimizes extraneous signal from tissue surrounding the cervix. The fiber optic probe design optimizes shallow depth Raman signal. The probe consists of a 300µm source fiber beveled inward and six 300µm collection fibers surrounding a circular core, depicted in Fig. 9. The collection fibers are lined up opposite of the source fiber to reduce the depth of the intersection between excitation and Raman light. The excitation fiber contains a narrow bandpass filter to allow 785nm light to reach the tissue while preventing unnecessary light. Backscattered incident light is prevented from entering the collection fibers with a long pass filter while allowing Stokes Raman scattering through. Because the distance between the source fiber and collection fiber varies, as does the maximum depth acquired. The four fibers furthest from the source fiber collect shallower signal while the other two collection fibers collect slightly deeper, but still shallow-focused signal compared to a traditional 7 collection fibers around one source fiber probe. In comparison to other phenomena occurring simultaneously such as fluorescence, Raman is a weak event. To combat the low SNR, all six fibers were used instead of only the four shallowest focus fibers.

Raman Probe Depth Characterization

The maximum depth of the source and collection fibers was measured using a combination of muscle tissue and fat samples, which were meant to serve as representative tissues for optimizing probe measurements. A 3 mm slice of bacon fat was placed on a flat surface and measured with the probe using 1.5 second integration, 5 accumulations at 80 mW (785nm). Afterwards, a 300-micron slice of tissue was placed on the fat and measured again. Twenty-one layers of 300-micron tissue slices were placed atop the sample while

measuring Raman signal before placing the next slice. The spectra were processed and deconstructed into percent lipid signal and percent protein signal using a least squares method. Results (see below) were used to optimize imaging conditions for subsequent cervical studies.

Animal Model

Table 3. The number of mice used in each experiment

	Mouse Model			
	wtD15	**wtD19**	**LPS**	**RU486**
Raman Studies	6	8	7	12
Biomechanics Studies	8	8	6	5

Mice are a favorable animal model to study PTB caused by infection or premature progesterone withdrawal [12]. However, the mechanisms used to achieve each phase of cervical remodeling is different between mice and humans [6]. These small differences are outweighed by the many benefits of studying mice: reduced ethical and clinical barriers, replicable experimental results, lower cost, shorter gestational lengths, ease of breeding, and a well characterized immune system [13].

Four mouse models were studied: wild type mice with normal parturition at term gestation (WT – Model 1) and wild type mice with premature parturition induced by either lipopolysaccharide (LPS – Model 2) or mifepristone (RU486 – Model 3), a progesterone receptor antagonist that is capable of inducing labor in women and most animal models. The numbers of mice used per model for each experiment is noted in Table 3. Day 1 is defined as the day after conception and WT mice deliver at day 19.5 of gestation. Day 15 (control for WT and PTB models – Model 4) and day 19 mice were measured every two hours until the end of the study. For day 19 mice, this point would be delivery, but for day 15 mice, this would be the point that the last PTB model mouse delivered during the experiment. LPS mice represent infection/inflammation-mediated preterm birth. LPS, an endotoxin derived from the gram-negative bacteria, E. coli 055:B5, was administered via intrauterine injection on day 15. The mice were measured using Raman every two hours until delivery of the first pup. For biomechanical testing, however, LPS mice were sacrificed at 6 hours post-injection.

RU486 mice represent induced PTB via an abortifacient used clinically in women. Mice were injected on day 15 with Mifepristone, a progesterone receptor antagonist, via intraperitoneal injection. Originally, mice were measured every four hours until delivery. However, later it was decided that important cervical changes occurred between that time period and the protocol was amended to measure mice every two hours after injection until delivery. While WT mice typically deliver at day 19.5, LPS and RU486 mice delivery on average 12 and 24 hours after injection respectively. Some WT mice were injected with saline on day 15 to serve as a control.

Raman Measurement Protocol

Mice were anesthetized using an isoflurane chamber. The cervix was gently washed with saline solution and softly dabbed with a cotton swab. A small speculum was placed inside the vagina to allow for visualization of the cervix and appropriate placement of the Raman probe on the clockface pattern (Fig. 10). The 2mm diameter probe was gently placed onto the surface of the cervix, perpendicular to the surface and overhead lights were turned off. A 1.5 second integration, 5 accumulation measurement was taken at 4 different locations of the cervix using a 785nm laser source at 80mW. This metric was chosen after performing an optimization study to lower the chance of saturation while maintaining an acceptable signal. As described earlier, if the cervix is visualized as a clockface, the measurement sites for the Raman probe are at 12, 3, 6, and 9 o'clock (Fig. 10). If a measurement appeared saturated by fluorescence, the angle of the probe was adjusted. If the problem persisted, the cervix was gently lavaged and swabbed again to remove any vaginal secretions. Following *in vivo* measurements, the mouse was sacrificed and the cervix excised for *ex vivo* measurements using the probe-based system. The cervix was placed standing upright on a piece of aluminum foil. If the cervix was unable to stand upright, the foil was bent slightly to provide support. A measurement was obtained from 3 different areas of the cervix to gather more complete information from the cervix. The cervix was then either prepared for biomechanical measurements or flash frozen and stored for future use.

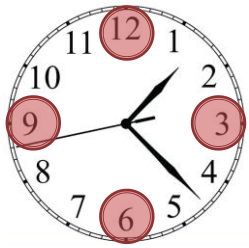

Figure 10. Visualization of the cervix as a clockface

Overnight experiments consisted of measuring mice every 2 hours from injection to delivery. A mouse was considered intrapartum after one pup was born.

Biomechanical Testing

Cervices were excised from intrapartum and 6-hour post injection mice. Measurements were taken of the height and width of the cervix; the cervix is shaped like a cylinder. Two small hooks were intertwined into the cervical os. One hook attached to a stationary hook that was placed into a prewarmed organ bath filled with oxygenated Krebs buffer where the cervix was allowed to acclimate for 10 minutes (Fig. 11). Afterwards, the other hook attached to a motor and force gauge and was threaded through the cervix which was stretched cyclically at .1mm/s for 10 seconds and then 4 minutes of rest. A stress-relaxation curve was then obtained until the cervix fractured. Before the first cycle began, the placement of the hook attached to the motor was recorded. Following fracture, the initial and maximum cervical dilation was obtained. The initial dilation was gathered after the cervix was removed from the system. The hook was moved back to the initial position recorded before the tension cycles began. At this point, the distance between hooks was measured using a ruler.

Figure 11. Hook system suspended above a heated bath

Biomechanical Analysis

Only data collected before the yield point was analyzed. As data collected directly from the tension testing system was in grams, the data was converted to Newtons. Stress was calculated from the resultant tension by dividing by the area of the cervix. Due to missing data points for RU486 mice, the area of the cervix was assumed to be similar to that of LPS mice. The area was the initial inner diameter of the cervix multiplied by the height. Stress-strain curves were developed for each mouse for both impulse and equilibrium. Impulse refers to the maximum point of each cycle minus the minimum point while equilibrium refers

to the mean of the last 5 seconds of the 4-minute phase of the cycle where the tissue has acclimated to the applied force. Some stress-strain curves did not follow the general trend of the others for that individual model and were thus removed from analysis. These samples were likely torn in the process of threading the tissue mounting hooks through the cervical canal. Median stress for the WT day 15, WT day 19, LPS, and RU486 models was calculated and an exponential trendline was fit to both equilibrium and impulse curves.

Raman Spectra Processing

Spectra were wavelength calibrated using a neon-argon lamp, acetaminophen, and naphthalene. Spectral intensity response was corrected for using a NIST standard tungsten lamp. Spectra were fluorescence subtracted using a 7^{th} order polynomial in a modified polynomial fit method developed in the Mahadevan-Jansen Lab [14]. Due to the low SNR of the spectra, some spectra showed etaloning effects. All spectra were manually checked for etaloning and spectra that did meet pre-defined criteria were removed. Spectra were mean normalized and imported into the R statistics package. A Principle Component Analysis (PCA) reduction was performed using 95% variance reduce noise in the spectra, which was then smoothed using Savitsky-Golay filter of polynomial order 2 and window size 9.

Spectral Analysis

Many variables were considered during spectral analysis including mouse model, lipid content in the signal, cervix location, measurement time, and time to delivery. There was a clear break in the spectra between normal signals and lipid rich signals. Thus, spectra were separated between spectra with a 1304 cm^{-1} peak intensity of higher than 2 c.u. and lower than or equal to 2 c.u. Peak ratios were calculated for individual mice throughout gestation and spectra were plotted with respect to time to delivery. Because even mice of the same PTB model varied between total delivery time, the time to delivery was also scaled from 0 to 100%. This was accomplished by dividing the current measurement time by the total labor time and multiplying by 100. The resultant value was then subtracted from 100. From this process, mice were considered to be 0% to delivery (or sacrifice in the case of WT day 15) at the injection or experiment start time and 100% to delivery at intrapartum. In addition to peak ratios, data was analyzed using principal component analysis (PCA). A PCA

model utilizes the entire Raman spectrum instead of a few specific peaks to classify samples. PCA helps to reduce the dimensionality of a complex data set; it reduces a set of high dimensional variables (wavenumbers) into a smaller set of variables called principle components (PCs) while retaining most of the information. The PCs obtained from PCA are defined with respect to the variance where PC1 demonstrates the maximum variance in the data. A scatter plot of two PCs can be used for outlier detection and identification of patterns in the data.

Seven peaks were selected for study, based on their relevance to the ECM: 1549, 1619, 1265, 1657, 1304, 1335, and 1440 cm^{-1}. Peaks at 1549 and 1619 cm^{-1} correspond to N-H scissoring/C-N bending and C=C stretch, respectively which has been attributed to tryptophan, tyrosine and heme [15,16]. Peaks at 1265 and 1657 cm^{-1} both correspond to protein[17,18]. However, 1265 cm^{-1} occurs due to CH in plane deformation attributed to amide III while 1657 cm^{-1} corresponds to mainly C=O stretching and has been attributed to amide I. In spectra of the mouse cervix, the peak at 1304cm^{-1} is associated with CH_2 twist/deformation in lipids and proteins[17]. When lipid signal dominates, the peak at 1304 cm^{-1} appears tall and narrow, but when contribution from lipids decreases, the peak becomes broader and shifts slightly to the right. 1440cm^{-1} shows CH2 deformation and can also be attributed to both lipids and proteins [19]. A lipid-heavy spectrum will show a tall, narrow band at 1440 cm^{-1}, while a protein-rich spectrum would have a peak shifted towards 1450 cm^{-1}. Protein and DNA are correlated with the 1335 cm^{-1} band attributed to CH_2 bending and nucleic acids (adenine/guanine) respectively [20,21].

Results

Depth Characterization of Raman Probe

The depth of the shallow-focus probe used in Raman studies was characterized using a layered model of thin chicken slices on top of fat. A least squares analysis was performed to separate the protein component from the fat component. As shown in Fig. 12, an exponential curve was fitted to the declining lipid signal. The lipid component weight reached 1/e^2 at a depth of 2.44 mm. This shallow depth probe makes obtaining a spectrum that is not overwhelmed by lipid signal possible (Fig. 13). However, this new probe displays a strong sapphire peak at 1064 cm^{-1}.

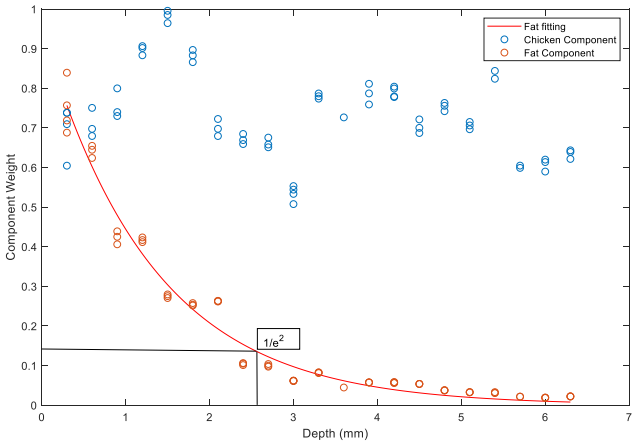

Figure 12. Depth profile of shallow focus probe

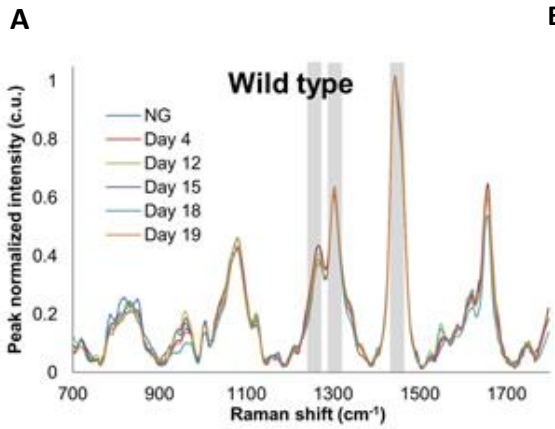

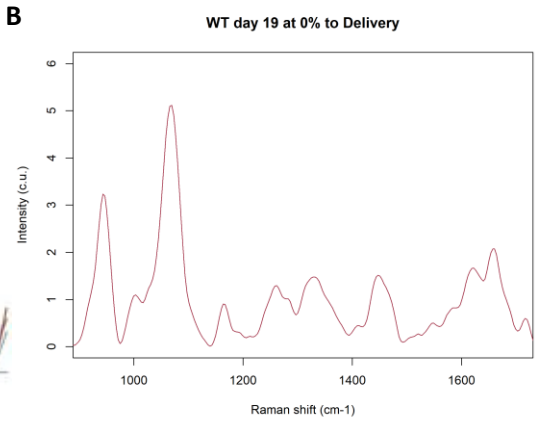

Figure 13. Comparison of (A) previous probe to (B) new shallow-focused probe

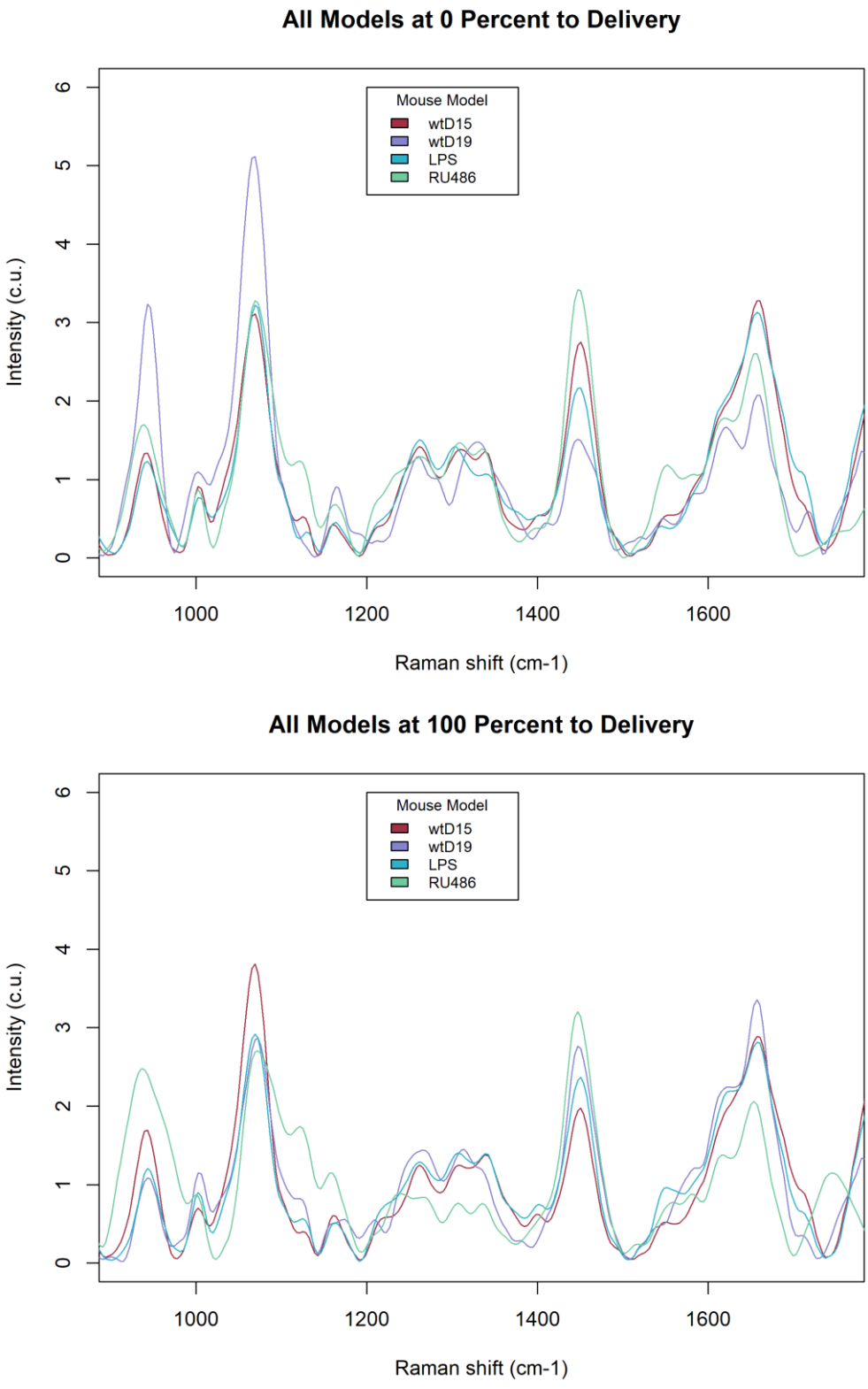

Figure 14. A representative spectrum of each mouse model at 0% and 100% to delivery

Table 4. A compilation of all Raman peaks studied

Peak Ratio	Mouse Model			
	wtD15	wtD19	LPS	RU486
1265	↓	broaden	↓	
1304	↓	↓		
1335			↑	↓
1549			↑	↓
1619		more pronounced peak		↓
1657	↓	↑	↓	↓
1265/1304			↓	
1265/1335	↓		↓	
1304/1335	↓		↓	↑
1549/1657	↑		↑	↓
1619/1549			↓	↑
1619/1657	↑		↑	

Raman Data Analysis

An example spectrum for each model at 0% and 100% to delivery is shown in Fig. 14, and all peaks studied are located in Table 4. There was very little overall change in the WT day 19 mice in comparison to the preterm birth models (Fig. 15 and 16). RU486 displayed the lowest signal to noise ratio (SNR) as shown in Fig. 15. Most RU486 spectra were categorized under the high lipid signal section during processing. Because of the low SNR, many of the remaining low-lipid RU486 spectra were removed from analysis. However, no interesting spectral changes were noted during a lipid-only analysis, strengthen the argument that lipid signal is indeed concealing other chemical changes that could be measured by Raman spectroscopy. At first, mice were individually plotted using an average of measurements from all locations of the cervix at a given time point. However, the standard error was unacceptably high when data from multiple clockfaces were analyzed together. This result implies that there is a more pronounced heterogeneity within the cervix and thus further analysis was performed only on individual clockface locations at a time.

LPS mice displayed a decrease in the 1619/1549 cm^{-1} peak ratio, while an increase was seen in RU486 mice. The 1549 cm^{-1} band alone did not appear to change in WT day 19 but did in both PTB models (Fig. 15). The 1549 cm^{-1} peak decreased in RU486 but increased in LPS mice. WT day 15 mice showed some variability in the 1549cm^{-1} peak, indicating there may be some inherent variability that could be better accounted for with a higher SNR signal from RU486. Since LPS induced PTB is an inflammation-mediated process and 1549 cm^{-1} is a Raman peak correlated with blood, it can be postulated than an inflamed cervix could be the cause of the higher peak ratio in LPS. The reason 1549 cm^{-1} was stable for WT day 19 may be attributed to the cervix having already undergone vascular changes in the previous 4 days. In contrast, 1619cm^{-1} has been correlated with porphyrins from blood, indicating that the 1549/1619 cm^{-1} ratio should remain stable in all mice regardless of blood flow [22]. This indicates there may be another biochemical mechanism that also presents at one of these two bands on the spectrum. In LPS treated mice, the 1619 cm^{-1} peak appears to become more pronounced, while it remains less noticeable in the WT day 15 control. Furthermore, the peak is already pronounced by the beginning of day 19 for WT mice.

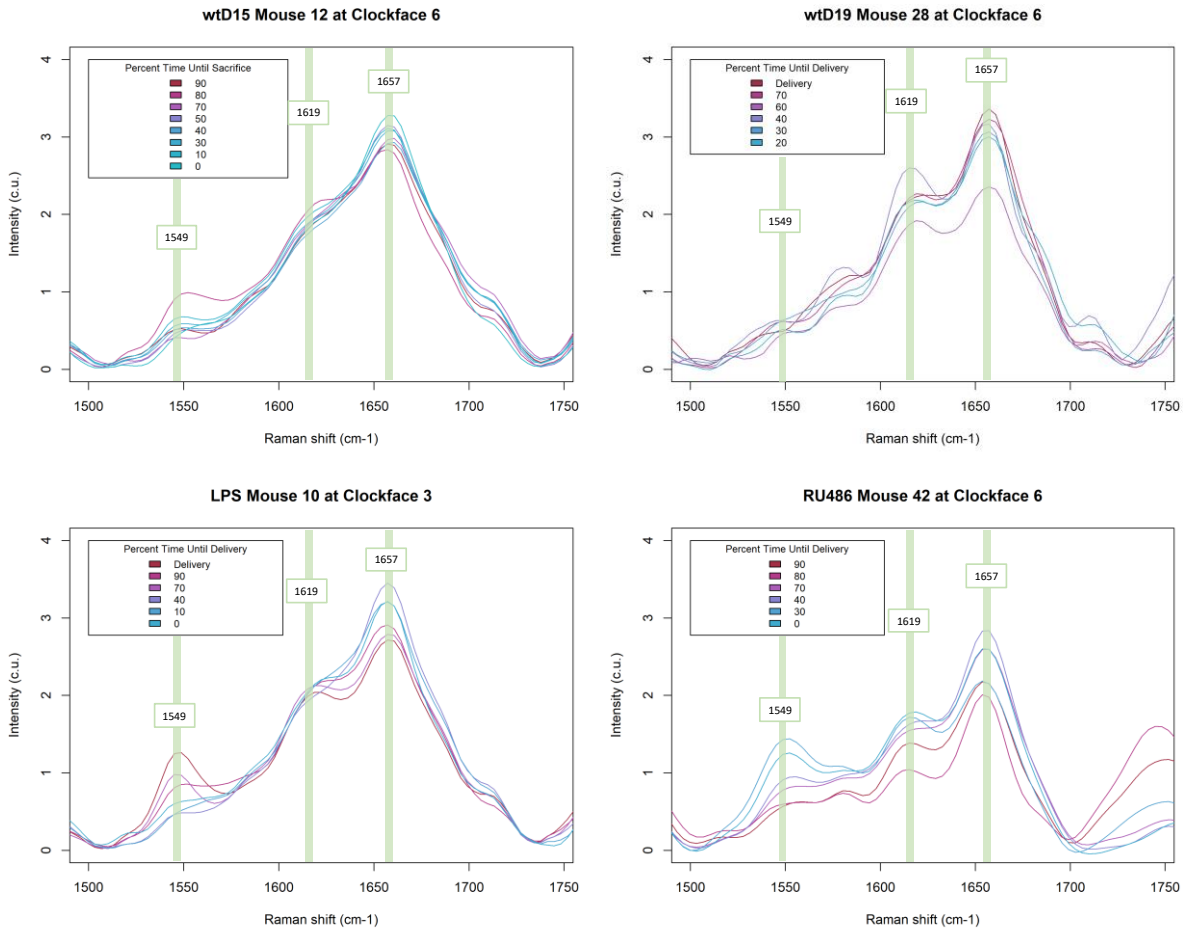

Figure 15. Raman spectra from 1500-1750 cm^{-1}

The 1657 cm^{-1} band associated with collagen appeared to decrease slightly in the WT day 15 control and both PTB models. However, the WT day 19 model displayed a slight increase in intensity at that band. This could mean that term WT mice undergo a change in collagen structure during cervical softening that reverts during the ripening phase. However, this explanation does not agree with the assumption that the 1657 cm^{-1} peak would decrease due to dissociation of collagen during cervical ripening. The 1619/1657 peak ratio remained constant in the WT day 19 and RU486 models but increased in WT day 15 and LPS. Similarly, WT day 15 portrayed a slight increase and LPS mice showed a substantial increase in the 1549/1657 ratio. While the ratio remained stable in WT day 19 mice, it appeared to slightly decrease in RU486 treated mice.

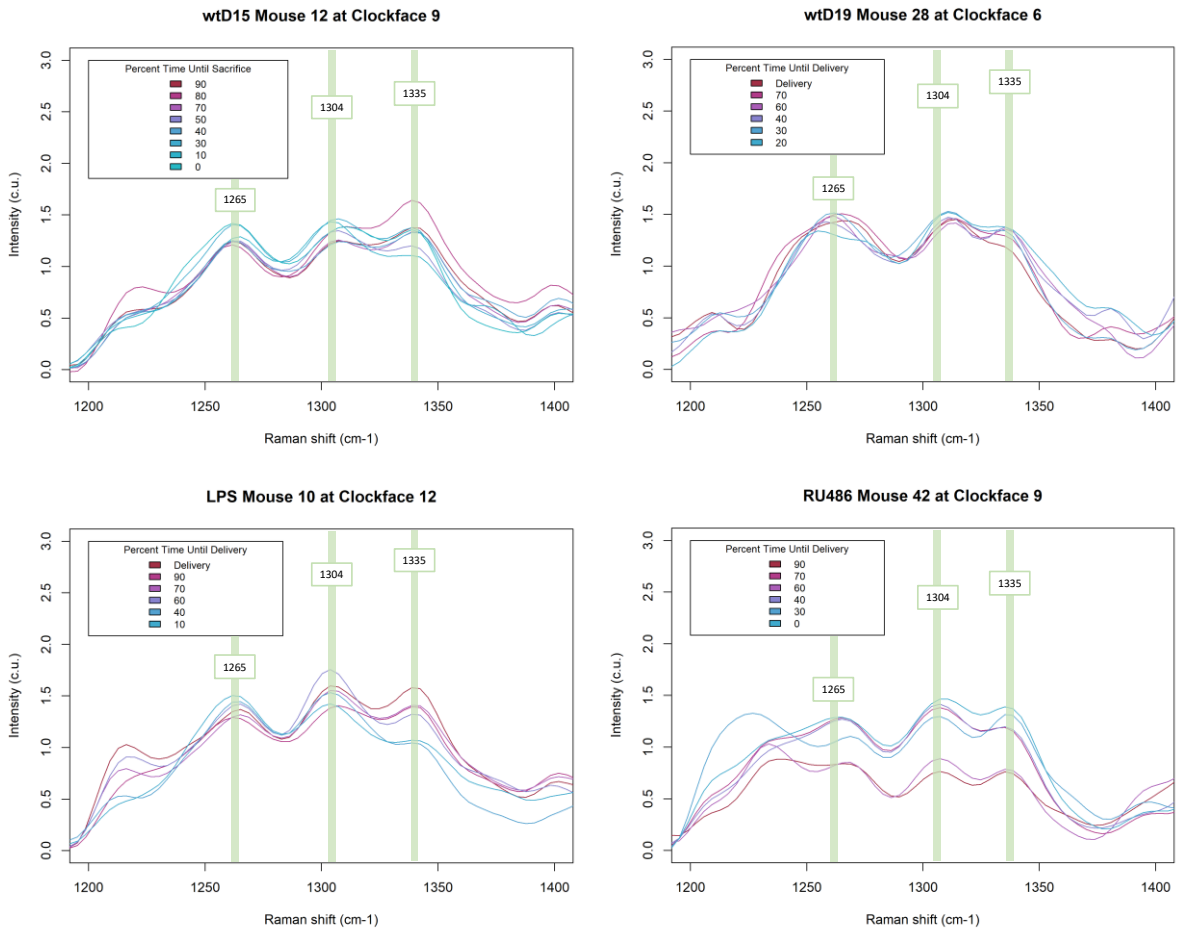

Figure 16. Raman spectra between 1200-1400 cm^{-1}

The 1440 cm^{-1} peak was noticeably taller and narrower in RU486 than the other models. This corroborates the fact that most measurements in RU486 were lipid heavy. However, in the RU486 model, some measurements at the beginning of experiments showed a broader, shorter 1440 cm^{-1} peak than the other three models at that time point. This discrepancy between RU486 and the control could be due to the low SNR of the RU486 spectra. here is a slight increase and thinning of the 1440 cm^{-1} peak in WT day 19 mice, which could be significant.

The 1265 cm^{-1} band decreased in the LPS model and the WT day 15 control. In WT day 19 mice, the intensity remained stable, but the band broadened slightly (Fig. 16). In addition, the starting value of in day 19 mice was like the value at the endpoint of day 15

control experiments, and higher than in LPS mice. In all mice, a decrease in collagen signal is expected due to the dissociation of cross-links during cervical ripening, which is required to achieve delivery [11]. This decrease in amide III bands at 1265 cm^{-1} suggests that collagen disorganization has already begun in WT day 15 mice, and an infection-mediated response speeds up this process. In all mice, there is a noticeable peak near the 1304 and 1335 cm^{-1} bands, attributed to lipid/protein and DNA/protein, respectively [22]. However, in RU486 injected mice, the peaks were shifted slightly to the right. The 1304/1335 peak ratio changed for both PTB models and the WT day 15 model. In both the day 15 control and LPS model, the ratio decreased, but in the RU486 model it increased. However, the contradictory peak ratio at RU486 may be due to the low SNR of the spectra. This variability makes it difficult to infer significance between the peak changes between 1200 and 1400 cm^{-1} for RU486 treated mice. Additionally, the 1265/1335 peak ratio decreased for both LPS and day 15 control mice. However, the ratio change appears more dramatic in LPS mice, as would be expected.

Principle Component Analysis

PCA analysis was conducted to determine the variability of the Raman spectra (Fig. 17-19). At the beginning of the study, the variability between WT day 15 and the PTB models showed a larger range of variability than the WT day 19 (Fig. 17). One important variable noted is the difference between spectra on a day-to-day basis. In particular, the RU486 model had one measurement date that held outliers in comparison to both other RU486 mice and other models (Fig. 18). While one date is different than the other for RU486, because of the limited data from low signal measurements, that date was not removed from analysis. As shown in the Raman data, there is a change in spectra that occurs throughout the duration of labor. This is also depicted in Fig. 19.

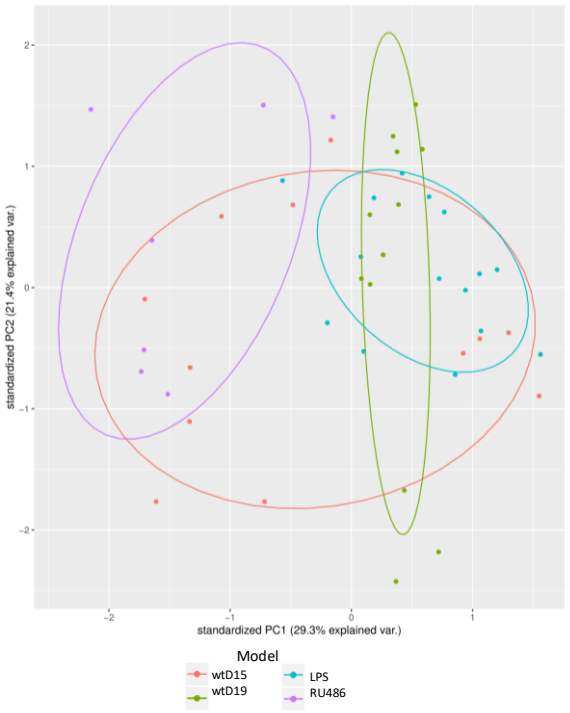

Figure 17. A PCA of all models at initial measurement for experiment

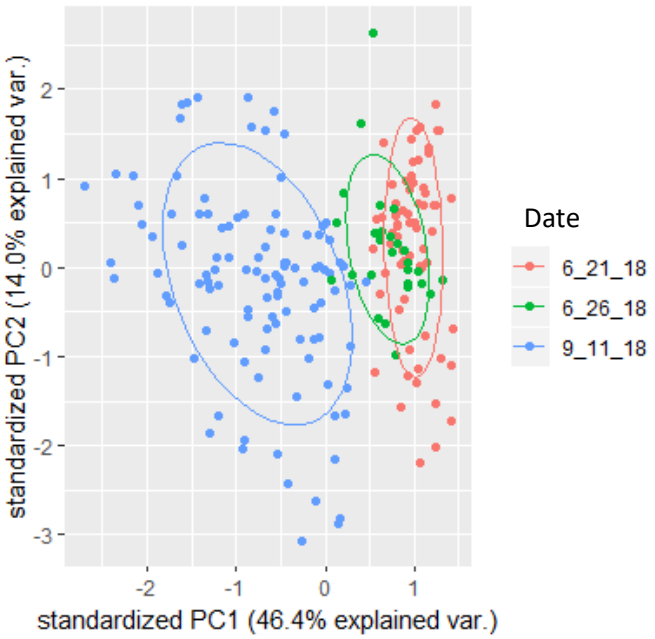

Figure 18. PCA of RU486 mice across different measurement dates

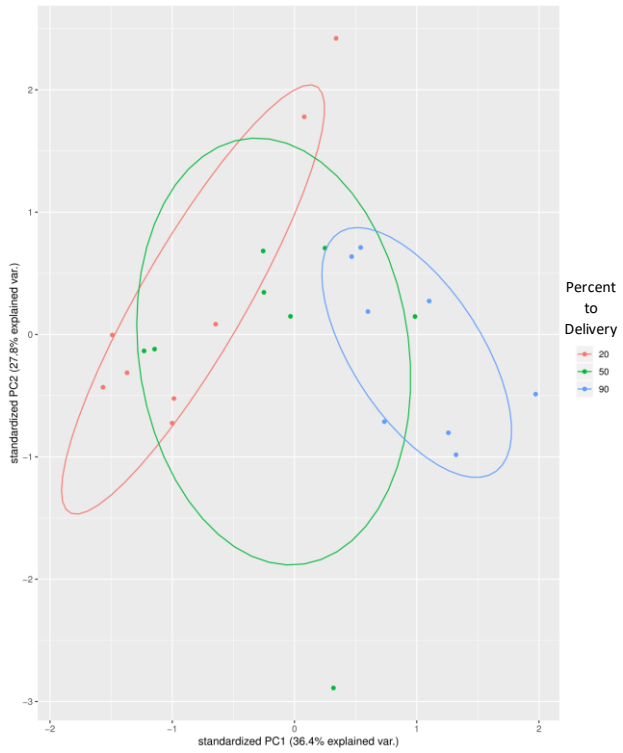

Figure 19. PCA of LPS spectra through the course of pregnancy

Biomechanics of the term and preterm cervix

An exponential trendline was calculated for all four mouse models and is shown in Fig. 20. In both the impulse and equilibrium curves, the WT day 15 cervix endured the most stress, with LPS coming in 2nd, then RU486, and WT day 19 facing the least amount of stress at any given time. Incidentally, the greatest change in dilation followed the same pattern (Fig. 21). LPS and WT day 15 mice tended to show similar trends in the Raman data. While there is a large degree of separation, the LPS model showed the most similar biomechanics results to the WT day 15 mice as well. As collagen provides strength to the cervix and is expected to become disassociated during cervical ripening, it is expected that at-term mice would have more elastic cervices. Raman data agrees with the biomechanical data with the decrease in 1265 cm^{-1} in LPS, but the Raman data for RU486 treated mice is inconclusive. While in the Raman data, LPS displayed the lowest 1265 cm^{-1} peak of all mice right before delivery, at 6 hours post-injection, the 1265 cm^{-1} had not decreased by much. This observation also agrees

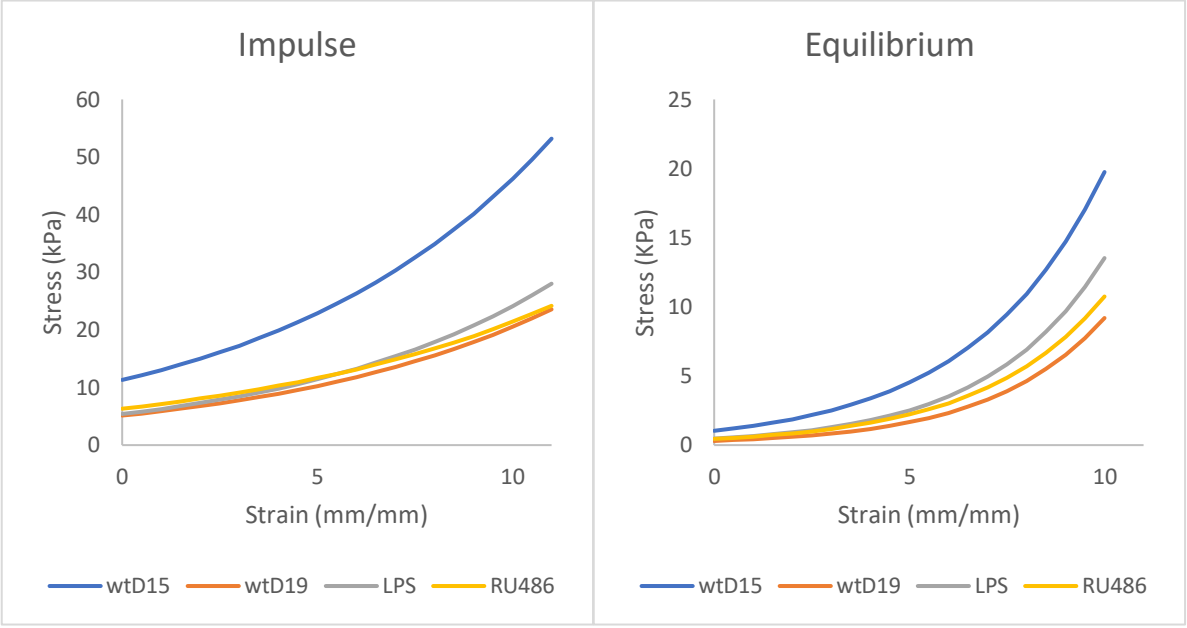

Figure 20. Stress-strain curves for impulse and equilibrium

with the fact that WT day 19 mice stretched further than LPS at 6 hours post-injection. RU486 mice would be expected to progress further as they were sacrificed 12 hours after injection. These time points were chosen because they are the average halfway point for each respective model, but it would be interesting to see the results of biomechanical testing on RU486 mice sacrificed 6 hours after injection.

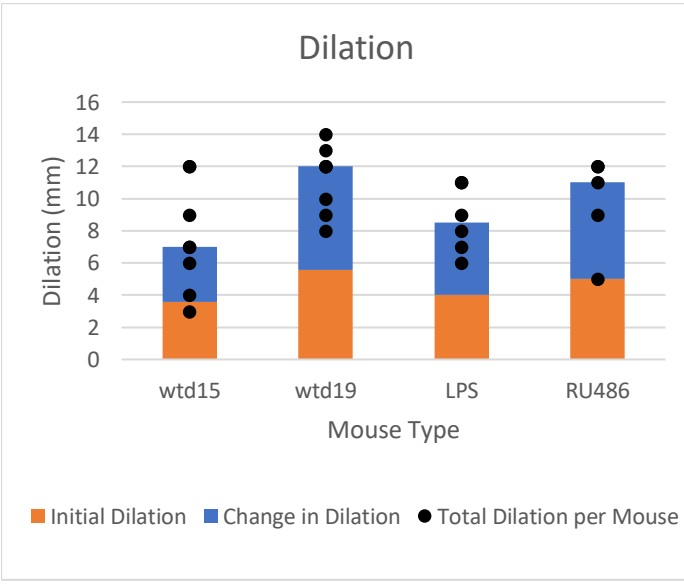

Figure 21. Change in cervical dilation throughout biomechanical stress testing

Discussion and Conclusions

This study analyzed the cervix of term and preterm birth mouse models to distinguish discrepancies between biochemical changes that could aid prediction of PTB. Raman spectroscopy was used to assess WT (normal cervical remodeling), LPS (inflammation-mediated cervical remodeling), and RU486 (induced cervical remodeling) models, in addition to biomechanical testing.

Interestingly, spectra of LPS mice showed a broader range of biochemical changes throughout pregnancy. However, LPS cervices were also the least flexible apart from the WT control during biomechanical testing. RU486 takes on average, 24 hours from injection on day 15 to delivery and WT day 19 have undergone 4 more days of cervical ripening than PTB models while mice infected with LPS endure a labor that only lasts an average of 12 hours. It is worth noting that mice pups delivered prematurely are much smaller than full term infants. It could be possible that full cervical ripening is unnecessary for LPS mice. It could also be possible that the inflammatory response indicated by the increased blood shown in LPS spectra could also render the cervix much less pliable during biomechanical stretch despite undergoing significant spectral changes.

While this study focused on changes within protein, lipid, and blood signal, studies show that the ripening cervix undergoes other changes including water content. Future studies should include a method to obtain water content. Previous research has shown high wavenumber Raman spectroscopy can accomplish this task[23,24]. Furthermore, studies have shown that wet weight is not an accurate method to analyze water content of the cervix [23,25]. Elastin, which plays a role in cervical remodeling, has also proven to be difficult to isolate from other proteins using Raman spectroscopy in the 1000-1800 cm^{-1} region. It may be possible to detect an upstream biochemical signal that indicates the creation of elastin, what that signal would be is currently unknown.

In humans, the cervix is known to be a homogenous organ [26]. Based on the variability of data between locations, our data displayed a heterogeneity of the mouse cervix. However, it is unknown if the heterogeneity seen in the Raman measurements is due to the cervix or interference from the surrounding tissue. While the probe used for these studies only

reaches a depth of less than 2.5 mm, much shallower than previous Raman probes that reached centimeters of depth, the mouse cervix is only 4 mm wide and 5 mm long. A further study to determine the source of heterogeneity would be helpful in this research.

The 1657 cm^{-1} band was generally broader in all models except but the RU486 where the band ended around 1700 cm^{-1}. As RU486 mice should match WT day 15 mice at the beginning of the experiment, this shows that RU486 data may not be precise, as the low signal clearly affected the data. More information would be available if the RU486 measurements were of a higher SNR. For all future studies, steps should be taken to reduce optical etaloning from the CCD in all experiments. This could be achieved by changing the laser power, though it is not recommended as 80mW is already at the edge of what would normally be deemed acceptable in laser safety. The integration time and number of iterations could be optimized. The current integration-accumulation parameters of 1.5s 5acc were chosen at the beginning of this MS work. Now that there is more information about what the spectra should look like and how easily etaloning occurs with those parameters, the information provided by this research could help to choose new parameters.

This study has shown the potential of using Raman spectroscopy to study cervical remodeling. Important spectral indicators were identified correlating to protein, DNA, lipid, and blood biochemistry. Furthermore, this study has indicated that important biochemical changes occur in between day 15 and day 19 for WT mice; it is possible that a day 17 mouse model would correlate more similarly to PTB models. Interestingly, though RU486 injected mice take on average 24 hours to deliver, at the midway point, they have progressed much further than LPS infected mice at 12 hours. This contradiction indicates further study into each abnormal cervical remodeling pathway is necessary to better understand precursors of PTB.

References

1. Bwtek. Components of a Raman Spectrometer. 2019.
2. Zone TP. 40 Weeks Pregnant. 2019; https://www.thepregnancyzone.com/pregnancy-weeks/40-weeks-pregnant/.
3. Clinic M. Cervical effacement and dilation. 2019; https://www.mayoclinic.org/healthy-lifestyle/labor-and-delivery/multimedia/cervical-effacement-and-dilation/img-20006991.
4. Word RA, Li X-H, Hnat M, Carrick K. Dynamics of cervical remodeling during pregnancy and parturition: mechanisms and current concepts. Paper presented at: Seminars in reproductive medicine2007.
5. *Hacker & Moore's essentials of obstetrics and gynecology.* Sixth edition. ed. Philadelphia, PA: Elsevier; 2016.
6. Timmons B, Akins M, Mahendroo M. Cervical remodeling during pregnancy and parturition. *Trends in Endocrinology and Metabolism.* 2010;21(6):353-361.
7. Baggish MS. *Atlas of pelvic anatomy and gynecologic surgery.* Fourth edition. ed. Philadelphia, PA: Elsevier; 2016.
8. Centers for Disease Control and Prevention. Preterm Birth. 2018; https://www.cdc.gov/reproductivehealth/maternalinfanthealth/pretermbirth.htm.
9. Feltovich H, Hall TJ, Berghella V. Beyond cervical length: emerging technologies for assessing the pregnant cervix. *Am J Obstet Gynecol.* 2012;207(5):345-354.
10. Vargis E, Tang YW, Khabele D, Mahadevan-Jansen A. Near-infrared Raman Microspectroscopy Detects High-risk Human Papillomaviruses. *Transl Oncol.* 2012;5(3):172-179.
11. O'Brien CM, Herington JL, Brown N, et al. In vivo Raman spectral analysis of impaired cervical remodeling in a mouse model of delayed parturition. *Sci Rep.* 2017;7(1):6835.
12. Holt R, Timmons BC, Akgul Y, Akins ML, Mahendroo M. The molecular mechanisms of cervical ripening differ between term and preterm birth. *Endocrinology.* 2011;152(3):1036-1046.
13. Shynlova, Lye OSJ. Labor and Preterm Labor. In:2014:751-753.
14. Lieber CA, Mahadevan-Jansen A. Automated method for subtraction of fluorescence from biological Raman spectra. *Appl Spectrosc.* 2003;57(11):1363-1367.
15. Nie S, Bergbauer KL, Kuck JFR, Yu N-T. Near-infrared Fourier transform Raman spectroscopy in human lens research. *Experimental Eye Research.* 1990;51(5):619-623.
16. Boustany NN. Absorption coefficient and purine photobleaching rate in colon mucosa during resonance Raman spectroscopy at 251 nm.(Abstract). *Applied Optics.* 2001;40(34):6396.
17. Frank CJ, McCreery RL, Redd DC. Raman spectroscopy of normal and diseased human breast tissues. *Analytical chemistry.* 1995;67(5):777.
18. Ozaki Y, Storer AC, Carey PR. The Raman and resonance Raman spectra of some substituted dialkyl dithioesters and their rotational isomers. *Canadian Journal of Chemistry.* 1982;60(2):190-198.

19. Manoharan R, Wang Y, Boustany NN, et al. Raman spectroscopy for cancer detection: instrument development and tissue diagnosis. In. Vol 23281994:128-132.
20. Zonios GI, Cothren JRM, Arendt J, et al. Fluorescence spectroscopy for colon cancer diagnosis. In. Vol 23711995:66-70.
21. Mahadevan-Jansen A, Mitchell MF, Ramanujam N, Utzinger U, Richards-Kortum R. Development of a Fiber Optic Probe to Measure NIR Raman Spectra of Cervical Tissue In Vivo. *Photochemistry and Photobiology.* 1998;68(3):427-431.
22. Bergholt MS, Zheng W, Lin K, et al. Characterizing variability in in vivo Raman spectra of different anatomical locations in the upper gastrointestinal tract toward cancer detection. *J Biomed Opt.* 2011;16(3):037003.
23. Masson LE, O'Brien CM, Pence IJ, et al. Dual excitation wavelength system for combined fingerprint and high wavenumber Raman spectroscopy. *Analyst.* 2018;143(24):6049-6060.
24. Duraipandian S, Zheng W, Ng J, Low JJH, Ilancheran A, Huang Z. Effect of hormonal variation on in vivo high wavenumber Raman spectra improves cervical precancer detection. In. Vol 82142012:82140A-82140A-82146.
25. Nallasamy S, Mahendroo M. Distinct Roles of Cervical Epithelia and Stroma in Pregnancy and Parturition. *Seminars in Reproductive Medicine.* 2017;35(2):190-199.
26. Vargis E, Byrd T, Logan Q, Khabele D, Mahadevan-Jansen A. Sensitivity of Raman spectroscopy to normal patient variability. *J Biomed Opt.* 2011;16(11):117004.

Chapter III

CHALLENGES AND FUTURE DIRECTIONS

Findings of this study indicate that Raman spectroscopy is a sensitive technique that can potentially measure biochemical changes in the cervix which in turn could be related to the cervical modeling that occurs with term and preterm pregnancy. While the current study focused on the fingerprint (800-1800 cm^{-1}) region of Raman spectra, illustrating changes within protein, lipid, and blood signal, other studies have revealed that the ripening cervix undergoes other crucial changes including tissue hydration (water content) [1]. Future studies could include a method to assess the water content (tissue hydration) of cervix during tissue changes associated with pregnancy. Previous research has shown that the high wavenumber region of Raman spectra (2600-3800 cm-1) can provide information about the water content (O-H stretch) in addition to C-H/N-H stretch mainly attributed to proteins and lipids [1,2]. In practice, the high wavenumber Raman spectra can be obtained using the same Raman system by switching the excitation wavelength to 680nm using a dual wavelength laser in combination with a broad bandpass filter in the probe that allows tissue or sample excitation with both 680 and 785nm [1]. This dual wavelength system therefore would have the potential to provide *in vivo* tissue water quantification in addition to other biochemical changes acquired at 785 nm.

Apart from collagen, elastin is responsible for elasticity in tissue and thus also would play a key role in cervical remodeling. However, due to spectral overlap with other proteins, it has been challenging to isolate elastin signatures in 1000-1800cm^{-1} Raman spectral region. This limitation can be offset in future studies, by also including tissue spectra from the 500-1000 cm^{-1} region for analysis [3]. Raman spectral features below 1100 cm^{-1} were obscured in the present study due to the probe background arising from the sapphire lens used in the current probe design. A factor to be considered for future studies, would involve replacing the current lens with a high-grade sapphire lens (A.W.I. Industries Inc, USA), which in recent studies has not produced interference between the 500-1800 cm^{-1} Raman spectral region [4]. The redesigned probe with the high-grade sapphire lens could then be used to acquire

Raman spectra that includes the isolated elastin Raman band at 527 cm^{-1} [3]. In this manner, spectral information pertaining to tissue hydration and elastin content can be obtained to augment information obtained with Raman spectroscopy, which can thus help in improving the accuracy and understanding of the biochemical mechanism of term and preterm cervical remodeling.

Data obtained with the present study was suggestive of heterogeneity in the mouse cervix, unlike human cervix which, on a macro scale, has appeared as a homogenous organ in Raman spectra [5]. However, due to interference from probe background and enhanced lipid signals, it was challenging to verify if the heterogeneity seen in Raman measurements were due to changes in the cervix or interference from adjacent tissue structures (e.g. pelvic or intraperitoneal fat). A key solution to solve this issue involved using a shallow-depth probe as described in Chapter 2 that would focus at a tissue plane less than 2.5 mm deep and hence should theoretically pick spectral signatures only from the cervical tissue. While the plane-of-focus with the described probe was much shallower than that obtained with the previous traditional Raman probes, it was found that the angle at which probe is inserted through speculum also affected the extent of signals collected from the surrounding tissues. Further studies that determine the source of heterogeneity in the acquired Raman spectra would be beneficial for this research. Additionally, poor SNR with the current probe design led to rejection of several spectra from final analysis. Going ahead, steps should be taken to reduce optical etaloning in the CCD for all Raman spectral measurements. This could be achieved by increasing integration time and by improving SNR by using a high numerical aperture lens to achieve better collection of Raman signals. At the beginning of this thesis work, current integration-accumulation parameters of 1.5 seconds at 5 accumulations were chosen based on findings from previous studies. However, more information has since then been obtained regarding how an 'ideal' Raman spectra from mouse cervical tissue should appear using a shallow-focus probe and how etaloning in the CCD can be minimized, providing future studies with the scope to choose and optimize new acquisition parameters for probe-based Raman spectroscopy.

To summarize, this study has demonstrated the potential of using Raman to study cervical remodeling in term and preterm parturition. Important spectral indicators were

identified and correlated to specific Raman spectral changes in protein, DNA, lipid, and blood biochemistry, alongside biomechanical changes in cervix including stiffness and distensibility in different models. The main novelty of this study revolved around using a newly designed Raman probe to acquire tissue information pertaining to all the relevant biochemical changes (collagen cross-linking, lipid, DNA, heme) that occurred in the cervix of inflammation-mediated and induced PTB. The ability to sense these changes from the mouse cervix with a single measurement in real-time, indicates clear potential for direct clinical translation of this technology for monitoring PTB.

References

1. Masson LE, O'Brien CM, Pence IJ, et al. Dual excitation wavelength system for combined fingerprint and high wavenumber Raman spectroscopy. *Analyst.* 2018;143(24):6049-6060.
2. Duraipandian S, Zheng W, Ng J, Low JJH, Ilancheran A, Huang Z. Effect of hormonal variation on in vivo high wavenumber Raman spectra improves cervical precancer detection. In. Vol 82142012:82140A-82140A-82146.
3. You AYF, Bergholt MS, St-Pierre J-P, et al. Raman spectroscopy imaging reveals interplay between atherosclerosis and medial calcification in the human aorta. *Science Advances.* 2017;3(12):e1701156.
4. Mo J, Zheng W, Huang Z. Fiber-optic Raman probe couples ball lens for depth-selected Raman measurements of epithelial tissue. *Biomedical Optics Express.* 2010;1(1):17-30.
5. Vargis E, Byrd T, Logan Q, Khabele D, Mahadevan-Jansen A. Sensitivity of Raman spectroscopy to normal patient variability. *J Biomed Opt.* 2011;16(11):117004.